Inorganic Chemistry

pubs.acs.org/IC
Article

Chemical Bonding Trends in $Y_2M_3Si_5$ (M = Mn−Cu, Tc−Pd, Re−Pt): A Study within the Broad $R_2M_3X_5$ Intermetallic Family

Giorgio Palla, Linda S. Reitz, Riccardo Freccero,* Serena De Negri, and Richard Dronskowski

Cite This: *Inorg. Chem.* 2025, 64, 21067−21075

ABSTRACT: A comparative analysis of the chemical bonding in the $Y_2M_3Si_5$ (M = Mn−Cu, Tc−Pd, Re−Pt) intermetallic compounds is presented, aiming at elucidating the chemical factors governing their crystallization into tetragonal ($tP40$−$Sc_2Fe_3Si_5$), monoclinic ($mS40$−$Lu_2Co_3Si_5$), or orthorhombic ($oI40$−$U_2Co_3Si_5$) structures. This study provides the first comprehensive bonding investigation of $Y_2M_3Si_5$ compounds with M = Fe, Co, and Ni, each adopting one of the three structure types. Employing projected crystal orbital Hamilton population curves (pCOHP), integrated pCOHP (IpCOHP), and integrated crystal orbital bond index (ICOBI) analyses, the bonding scenario is revealed to be primarily dominated by polar covalent M−Si interactions, followed by Y−Si, with Si−Si bonds playing a secondary role. This highlights a bonding picture more complex than that predicted by the Zintl concept. Extending the analysis to all transition metals and prototypes, regardless of their thermodynamic stability, allows for a systematic comparison of bonding in both stable and metastable configurations. The covalency distribution within the unit cell, quantified as IpCOHP%, exhibits periodic trends across the transition metal series, both along periods and down groups. The maximization of M−Si IpCOHP% emerges as the key chemical factor in stabilizing one structure type over another, aligning with experimental observations.

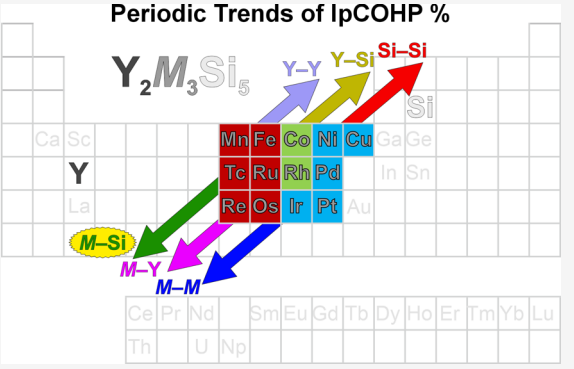

INTRODUCTION

Intermetallic compounds constitute one of the largest classes of inorganic materials,[1] characterized by a wide variety of crystal structures and elemental combinations, often giving rise to unique electronic structures and, consequently, distinctive physical and chemical properties.[2,3] While the former have been extensively investigated and remain the focus of several research groups, the latter have gained significant attention only in recent years, particularly in the field of heterogeneous catalysis.[3−11] This trend is also evident within the large $R_2M_3X_5$ family (R = rare earth metal/actinide, M = transition metal, X = p-block element from groups 13 and 14), which comprises more than 200 known representatives crystallizing in eight different structure types.[12,13] Superconductivity,[14,15] Kondo behavior,[16,17] giant magnetoresistance,[18] and charge density wave[19] are just a few examples of the broad range of physical properties, recently enriched by a strong potential for topological phenomena.[20] A detailed survey on $R_2M_3X_5$ compounds was recently published in the *Handbook on the Physics and Chemistry of Rare Earth*,[12] where the lack of data on their chemical bonding was highlighted. In fact, such results were available only for $La_2Pd_3Ge_5$ ($oI40$−$U_2Co_3Si_5$; SG: *Ibam*, No. 72),[21] as part of our comprehensive investigation of the $R_2Pd_3Ge_5$ series,[22,23] and were further complemented by a chemical bonding analysis of $La_2Pd_3Si_5$, the other endmember of the complete $La_2Pd_3(Si_xGe_{1-x})_5$ solid solution.[24] In both cases, the bonding analysis, primarily based on the crystal orbital Hamilton population (COHP)[25] and its integrated value (ICOHP), revealed a much more complex scenario than predicted by a straightforward application of the Zintl formalism. Indeed, the Pd−Si(Ge) contacts showed the highest ICOHP values, followed by the homopolar Si(Ge)−Si(Ge) contacts, with other previously overlooked interactions, such as La−Pd and La−Si(Ge), making significant contributions to the overall picture. Nevertheless, these results are clearly insufficient to address a key challenge for $R_2M_3X_5$ compounds, as pointed out by Brown et al.,[12] understanding the relationship between structure types and their bonding. In other words, it uncovers the chemical factors that drive their crystallization into a specific structure type. The subfamily of the silicides (X = Si) represents a suitable playground for this type of investigation, as they adopt different structures mainly depending on the nature of the M metal. In particular, the $tP40$-$Sc_2Fe_3Si_5$ structure (SG: $P4/mnc$, No. 128) is preferred

Received: July 18, 2025
Revised: September 15, 2025
Accepted: September 24, 2025
Published: October 13, 2025

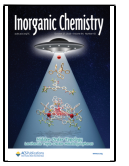

https://doi.org/10.1021/acs.inorgchem.5c03309
Inorg. Chem. 2025, 64, 21067−21075

with M elements from the Mn and Fe groups, whereas the $oI40$-$U_2Co_3Si_5$ is preferred with M metals belonging to the Co and Ni groups. The $mS40$-$Lu_2Co_3Si_5$ structure (SG: $C2/c$, No. 15) is mainly adopted by a few representatives with M from the Co group. This trend follows the valence electron count (VEC), as values lower than 50 lead to the $Sc_2Fe_3Si_5$-type, while those higher than 53 typically stabilize the $U_2Co_3Si_5$ structure. This is attributed to the fact that increasing the d-electron counts, which corresponds to increasing VEC, results in a gradual weakening of the M−M interactions, thereby assigning a significant role to these bonds in determining the structural preference.[12] Nevertheless, the VEC is insufficient to fully account for the observed structural preferences, making it unsuitable for predictive purposes, thus requiring experimental confirmation, as in the case of $Lu_2Co_3Si_5$, first reported as orthorhombic[26] ($oI40$-$U_2Co_3Si_5$ type) and subsequently revised as monoclinic[27] ($mS40$-$Lu_2Co_3Si_5$ type). Although it is reasonable to assume a polymorphic transition between the orthorhombic and monoclinic structures, given the existence of a direct group−subgroup relationship (see Figure S1), such a transition has so far been observed only for the $Pr_2Co_3Ge_5$ germanide.[28] These findings suggest that the two structures are stabilized by distinct bonding scenarios, despite their strong structural similarities, thus requiring in-depth investigations based on quantum−chemical methods.

Among all the $R_2M_3Si_5$, we selected those with R = Y as they have been reported with several transition metals M, making this series suitable for a comparative analysis. The distribution of their experimentally determined crystal structures across the different transition metals is schematically summarized in Figure 1.

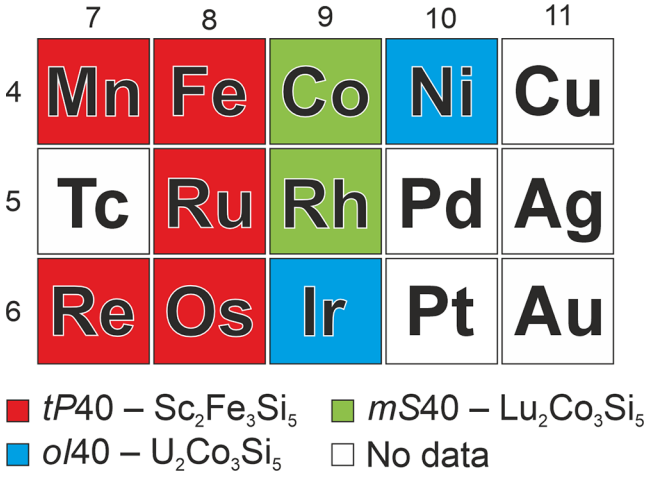

Figure 1. Distribution of the experimentally determined crystal structures of $Y_2M_3Si_5$ compounds depending on the nature of transition metal M.

The $tP40$ structure (red in Figure 1) is adopted when M belongs to the Mn and Fe groups,[14,29−31] the $mS40$ is observed with Co and Rh[27,32] (green), and the $oI40$ with Ir and Ni[33,34] (blue). Despite $Y_2M_3Si_5$ silicides forming with many M elements, no compounds have been reported so far with Tc, Pd, Pt, or Cu group metals (white in Figure 1). Notably, while Pd- and Pt-containing phases are known with early lanthanides, $R_2Cu_3Si_5$ has only been reported for R = Eu,[35] and no $R_2M_3Si_5$ compounds have been obtained with M = Ag, Au. Therefore, in this work, we focus on the $Y_2M_3Si_5$ (M = Mn−Cu, Tc−Pd, Re−Pt) compounds.

In the present work, the results are presented in two separate sections. In the first, we report the outcomes of the chemical bonding analyses performed on $Y_2Fe_3Si_5$, $Y_2Co_3Si_5$, and $Y_2Ni_3Si_5$, selected as representatives of the $tP40$-$Sc_2Fe_3Si_5$, $mS40$-$Lu_2Co_3Si_5$, and $oI40$-$U_2Co_3Si_5$ structure types, respectively. In the second section, bonding data derived from the calculated electronic structures of all selected $Y_2M_3Si_5$ compounds (M = Mn−Cu, Tc−Pd, Re−Pt), each modeled in the $tP40$, $mS40$, and $oI40$ structures, are presented and analyzed to identify the chemical driving forces that govern their structural preferences.

Computational Methods. All electronic DFT calculations were performed using the Vienna Ab-initio Simulation Package (VASP, version 5.4.4),[36−40] with the Projector Augmented Wave (PAW) method as first described by Blöchl.[41] The Perdew, Burke, and Ernzerhof (PBE)[42] exchange-correlation functional within the generalized gradient approximation (GGA) was employed. The energy cutoff for the plane waves was set at 500 eV in all cases. The Brillouin zone was sampled according to the Monkhorst−Pack[43,44] scheme, using the following k-point mesh for each investigated crystal structure: 10 × 8 × 14 ($oI40$), 8 × 8 × 14 ($tP40$), and 8 × 8 × 14 ($mS40$). A full structural relaxation, i.e., optimizing both atomic positions and lattice parameters, was performed for all three structural models across the compositions. The computations were considered converged when the energy differences between two iterative steps were below 10^{-7} eV for the electronic and 10^{-5} eV for the ionic relaxations. All calculations, except for $Y_2Mn_3Si_5$, were performed without spin polarization, as they were experimentally found to be superconductors or Pauli paramagnets.[14,26,30,33,45,46] Since $Y_2Mn_3Si_5$ displays a ferrimagnetic ground state (T_N = 96 K),[29] spin polarization was included; however, no significant differences in the chemical bonding results were found compared to the nonmagnetic case. Once the electronic structure of the materials was obtained, the plane-wave-based wave functions were reconstructed using the local orbital basis suite toward electronic structure reconstruction (LOBSTER, version 5.0.0)[25,47−50] code. The projection from a delocalized plane-wave-based wave function into localized atomic orbitals was performed using the pbeVaspFit2015[48] basis set, employing the recommended basis functions. Density-based effective charges (according to Bader) were derived from the VASP charge density output, as implemented in the Henkelman code,[51−54] and Löwdin charges were calculated using LOBSTER directly from the wave function.[48] This was combined with wave function-based bonding indicators also extracted by LOBSTER, namely the projected COHP (pCOHP),[25,47] and the crystal orbital bond index (COBI),[55] with their integrated values (IpCOHP, ICOBI). The threshold for including a selected interaction in the bonding analysis was determined by defining coordination polyhedra for each species based on the maximum gap method. Moreover, given the large number of different types of bonds present in the compounds, and the need to perform comparative analysis, the cumulative integrated pCOHP/cell, and their corresponding percentage values (ICOHP%) were evaluated and analyzed. This follows a well-established approach proven to be suited for conducting comparative bonding studies in intermetallic compounds.[56−60] The pCOHP and COBI curves were

https://doi.org/10.1021/acs.inorgchem.5c03309
Inorg. Chem. 2025, 64, 21067−21075

visualized with the wxDragon[61] program, and the structural models were generated by means of the VESTA[62] software.

RESULTS AND DISCUSSION

Chemical Bonding in $Y_2M_3Si_5$ (M = Fe, Co, Ni). $Y_2Fe_3Si_5$, $Y_2Co_3Si_5$, and $Y_2Ni_3Si_5$ were selected for in-depth chemical bonding analysis as representatives of the tP40-$Sc_2Fe_3Si_5$, mS40-$Lu_2Co_3Si_5$, and oI40-$U_2Co_3Si_5$ structures, respectively. More details on their crystallographic data are available in the Supporting Information (Tables S1–S3). In a first approximation, the chemical bonding can be described by applying the 8–N rule to the silicon sublattice. Assuming a formal charge transfer from both yttrium and the M metals to silicon and evaluating the presence of Si–Si covalent bonds based on interatomic distances, electroneutrality is respected for $Y_2Co_3Si_5$ and $Y_2Ni_3Si_5$ by the following ionic formula: $(Y^{3+})_2(M^{2+})_3[(0b)Si^{4-}][(2b)Si^{2-}]_4$ (b = bonded). As shown in Figure 2b,c, $(2b)$Si realizes infinite zigzag chains running parallel to [001]. The same does not apply to $Y_2Fe_2Si_5$ (tP40), given the occurrence of both $(1b)$ and $(2b)$Si, which yield an ionic formulation comprising excess electrons: $(Y^{3+})_2(Fe^{2+})_3[(1b)Si^{3-}][(2b)Si^{2-}]_4 \times 1e^-$. Increasing the number of electrons formally transferred from iron, i.e., assuming Fe^{3+}, would not help in fulfilling electroneutrality, resulting in electron deficiency. As shown in Figure 2a, $(1b)$ and $(2b)$ give rise to dumbbells and zigzag chains, respectively.

As already pointed out for several ternary rare-earth tetrelides,[63−65] including $La_2Pd_3Ge_5$ and $La_2Pd_3Si_5$,[21,24] these formal pictures are insufficient to account for the much more complex bonding scenario, which is generally characterized by polar–covalent, rather than ionic, interactions between the cationic and anionic partial structures. To provide a more quantitative description, Table 1 presents calculated effective charges (Q^{eff}) according to the quantum theory of atoms in molecules (QTAIM, left) and wave function-based Löwdin charges (right), supporting this evidence (Table 1, left).

As expected, all charges are far smaller than regular oxidation states, the usual phenomenon, because oxidation states are a rather formal issue, alluding to heteroatomic electron partitioning (on paper). Nonetheless, it is quite instructive and a bit puzzling, too, that the atomic charge assignments based either on the density (QTAIM, Bader approach) or on the wave function (Löwdin), both derived from exactly the *same* electronic ground state, arrive at different pictures, even though both cationic and anionic entities exist in both. Within QTAIM, the yttrium atom is the only cation, strongly charged (ca. +1.5e), while both transition metals and silicon appear as being anions, the transition metals even being more anionic (−0.7 ± 0.3e) than Si (−0.2 ± 0.2e). In the Löwdin representation, one finds cationic transition metals (ca. +0.46e) and anionic silicon (ca. −0.27e) in addition to practically neutral yttrium. It would be most interesting to see which of the two pictures is closer to an observable property, e.g., a chemical shift as determined by NMR. The DOS curves for all compounds show nonzero states at the Fermi level, confirming their metallic nature (Figure 3). Moreover, the Fermi level lies in a pseudogap for $Y_2Fe_3Si_5$ and $Y_2Ni_3Si_5$ (Figure 3a,c), deeper for the former, and in a region of lower DOS located between two relative maxima for $Y_2Co_3Si_5$ (Figure 3b).

The energy regions of the DOS dominated by the M states (gray lines in Figure 3a–c) correspond to their 3d orbital contributions. It is worth noting that as the d-electron count

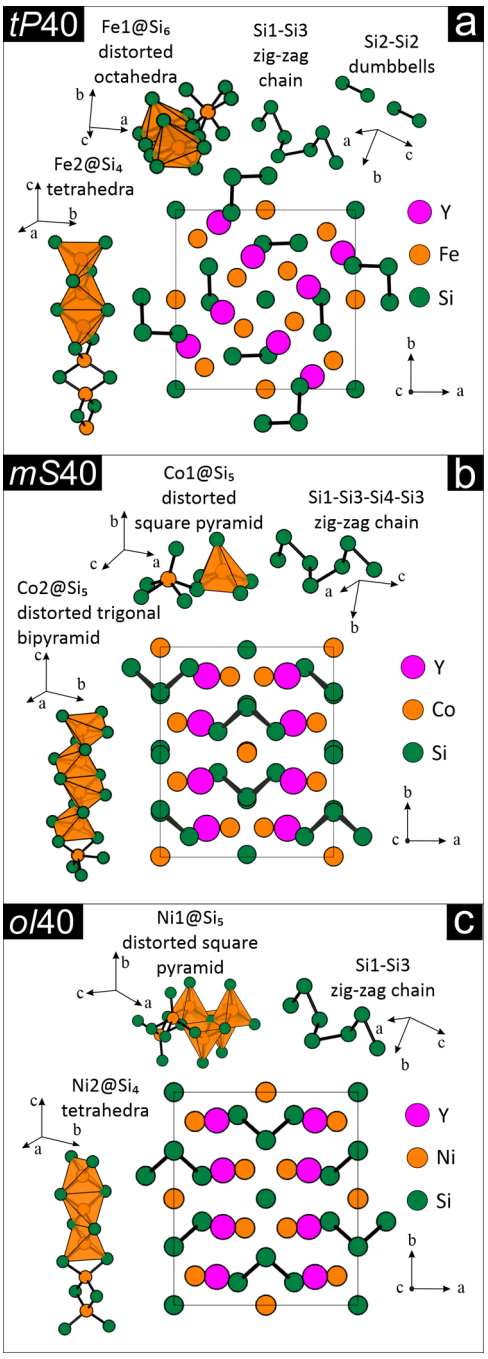

Figure 2. Crystal structures of (a) $Y_2Fe_3Si_5$, (b) $Y_2Co_3Si_5$, and (c) $Y_2Ni_3Si_5$ selected as representative for the tP40-$Sc_2Fe_3Si_5$, mS40-$Lu_2Co_3Si_5$, and oI40-$U_2Co_3Si_5$ types, respectively. Details on the Si-based polyanions, deduced according to interatomic distances, as well as the mutual coordination between Si and M are also provided.

Table 1. QTAIM Effective Charges for Each Constituent Atom Ω of the $Y_2M_3Si_5$ (M = Fe, Co, Ni) Compounds and the Corresponding Löwdin Charges from the Wave Function

	Q^{eff} (Ω)			Löwdin charge (Ω)		
	Y	M	Si	Y	M	Si
$Y_2Fe_3Si_5$	+1.47	−0.37	−0.36	−0.06	+0.40	−0.22
$Y_2Co_3Si_5$	+1.52	−0.78	−0.14	0.00	+0.42	−0.25
$Y_2Ni_3Si_5$	+1.53	−0.98	−0.09	+0.02	+0.56	−0.34

https://doi.org/10.1021/acs.inorgchem.5c03309
Inorg. Chem. 2025, 64, 21067−21075

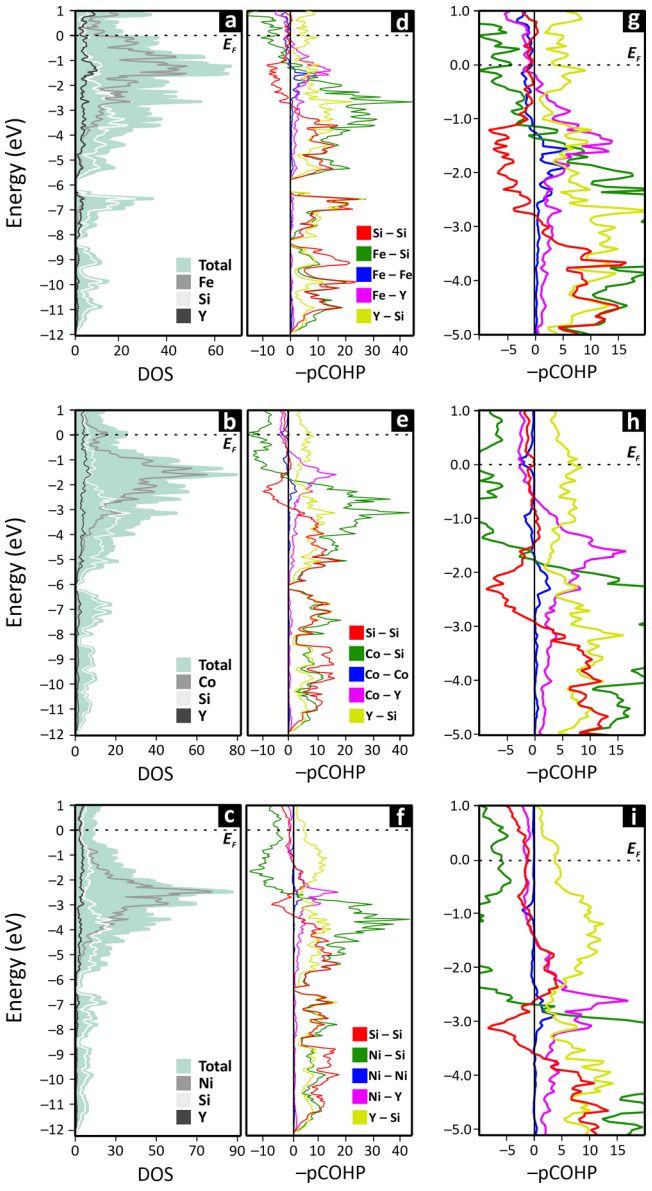

Figure 3. DOS (a−c) in units of (cell·eV)$^{-1}$ and pCOHP in units of (cell)$^{-1}$ (d−i) curves for the $Y_2Fe_3Si_5$ (*tP*40), $Y_2Co_3Si_5$ (*mS*40), and $Y_2Ni_3Si_5$ (*oI*40). To enable a better view, the pCOHP curves are also reported in the range from −5 to 1 eV (g−i). The Fermi energy is set at 0 eV. The Y−Y pCOHP curves are not shown due to their low values, which hinder clear visualization.

increases, the *d*-bands shift toward lower energies with a narrowing of their bandwidth, suggesting a gradual reduction in the extent of *M* involvement in covalent interactions. The Si 3*s* and 3*p* levels (light gray lines in Figure 3a−c) contribute to the region from about −12 to −6 eV, and from −6 eV to E_F, respectively. The latter shows a significant energetic overlap with the 3*d* *M* levels, supporting the covalent nature of the Si−*M* bonds. The Y states are dispersed over the entire considered energy range (dark gray lines in Figure 3a−c) with contributions from its 4*d*, particularly in the vicinity of E_F, supporting its partial ionization.

Focusing on the pCOHP curves (Figure 3d−i), it is noteworthy that despite structural differences, they all show similar trends. The pCOHP related to Si−Si interactions is predominantly bonding up to approximately −3 eV, resulting in integrated cumulative values (−IpCOHP, see Table 2) ranging from about 66 to 74 eV/cell. The values of IpCOHP per bond are listed in Table S4. This supports the covalent nature of these interactions and aligns with the previously presented formal description.

Table 2. Cumulative Integrated pCOHP (IpCOHP/cell) and Their Percentages to the Net Bonding Capacities (IpCOHP%/cell) for Each Type of Interaction within the Analyzed Compounds

	−IpCOHP (eV/cell)			IpCOHP%/cell		
$Y_2M_3Si_5$	Fe	Co	Ni	Fe	Co	Ni
M−*M*	4.55	1.67	0.91	1.35	0.53	0.29
M−Si	114.94	99.78	85.33	34.01	31.53	27.47
Si−Si	65.67	69.83	74.26	19.43	22.07	23.90
M−Y	26.67	29.11	24.19	7.89	9.20	7.79
Y−Si	121.36	112.86	123.02	35.91	35.66	39.60
Y−Y	4.77	3.19	2.96	1.41	1.01	0.95

At this point, it is worth underlining that within a Zintl framework, where covalent bonding occurs exclusively among Si atoms and ionic interactions take place between the Si substructure and the metal cations, the *M*−Si and Y−Si pCOHP curves would be expected to display narrow bands with low −IpCOHP.[47] As is clear from both Figure 3 and Table 2, this is not the case for the systems under investigation in this article. That being said, the numerical finding does not question the simplistic Zintl picture but emphasizes its model-like concept.

The *M*−Si curves (Figure 3g−i, dark green) switch from bonding to antibonding near E_F. The energy at which these transitions occur gradually decreases from Fe (−1.0 eV) to Ni (−2.5 eV), correlated with the increasing *d*-electron count. It may also be noted that this bonding−antibonding crossover coincides with the peaks in the pCOHP curves of the *M*−Y interactions (Figure 3g−i, purple) and in the DOS, corresponding to the half-filling of the *d* shell. The pCOHP of the Y−Si curves, contrary to the *M*−Si ones, are bonding up to E_F and above (Figure 3g−i, light green), clearly indicating the active involvement of Y in the chemical bonding, a feature also observed in other rare-earth ternary intermetallics.[21,24,66,67] Moreover, the Y−Si curves are the only ones featuring significant bonding contributions at E_F, compensating for the antibonding *M*−Si ones. Interestingly, the −IpCOHP for the Y−Si displays the largest values (>113 eV/cell), while the *M*−Si, which is second in the ranking of −IpCOHP, decreases from about 115 to 85 eV/cell with increasing the number of *d* electrons (−IpCOHP(*M*−Si): *M* = Fe > Co > Ni). The Y−*M*, *M*−*M*, and Y−Y interactions contribute considerably less to the overall bonding scenario. Nevertheless, although weak, Y−*M* and Fe−Fe support covalent interactions. To give additional insights, this bonding study is further complemented by the analysis of the ICOBI values (Figure 4), which enables a more accurate description of the nature of each interaction in terms of bond order. Note that ICOBI is the periodic equivalent of the Wiberg−Mayer bond order derived from the wave function, 1 for H−H, 1.5 for an aromatic C−C bond, 2 for O=O, and 3 for N≡N. Fractional bond orders (just like for benzene) are normal in intermetallic phases, the reason being the typical undersupply of electrons in metallic systems.

https://doi.org/10.1021/acs.inorgchem.5c03309
Inorg. Chem. 2025, 64, 21067−21075

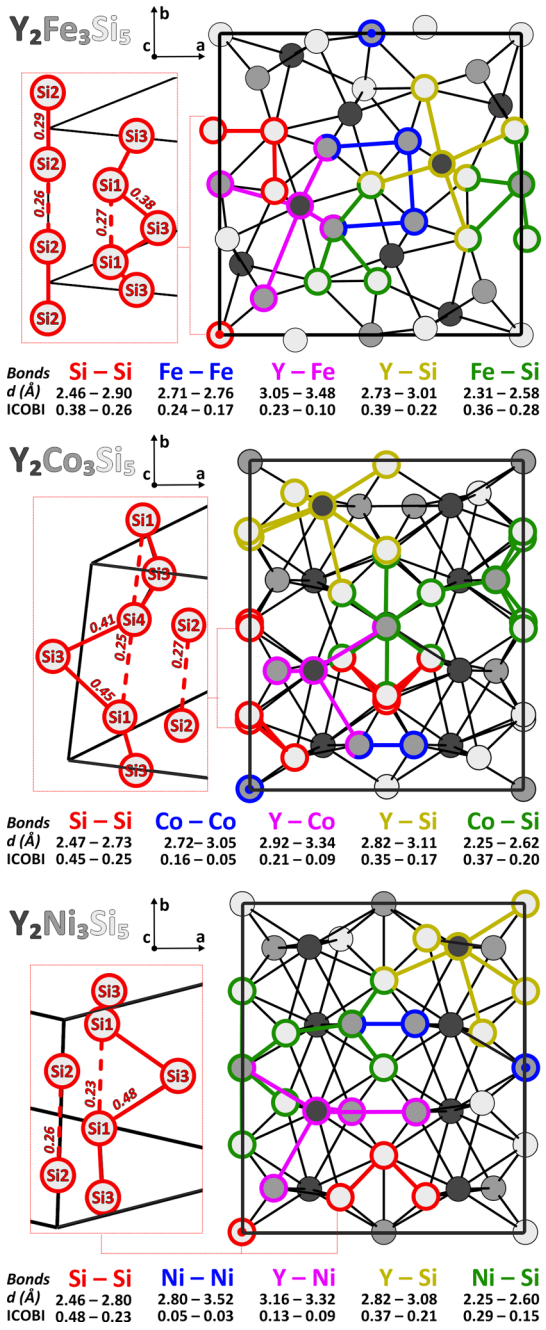

Figure 4. Crystal structures of the three studied compounds, viewed along the *c*-axis. Colored sticks indicate different types of contacts, for which both the distance ranges d(Å) and the corresponding ICOBI value ranges are reported. On the left side of each structure the Si polyanionic networks are shown, along with their ICOBI values. Dashed red lines indicate contacts that are not interpreted as covalent bonds according to the Zintl model.

For all structures, the largest ICOBI are related to all interactions, including silicon, i.e., Si−Si, Y−Si, and *M*−Si. The ICOBI for Y−Si and *M*−Si exceed the values expected for ionic interactions[55] also at quite long distances, e.g., for $Y_2Fe_3Si_5$ $ICOBI_{Y-Si}$(3.01 Å) = 0.22 and $ICOBI_{Fe-Si}$(2.58 Å) = 0.28, supporting the covalent character of these heteroatomic polar covalent interactions. At this point, it is worth focusing on the ICOBI for the Si−Si contacts. In all structures, the highest ICOBI values correspond to the shortest Si−Si distances, supporting the previously discussed partial structures: (2*b*)Si zigzag chains ($ICOBI(tP40)^{2.46\ Å}_{Si1-Si3}$ = 0.38, $ICOBI(mS40)^{2.47Å}_{Si3-Si4}$ = 0.41, and $ICOBI(mS40)^{2.49\ Å}_{Si1-Si3}$ = 0.45, $ICOBI(oI40)^{2.46\ Å}_{Si1-Si3}$ = 0.48) and (1*b*)Si dumbbells in the *tP*40 modification ($ICOBI(mS40)^{2.52\ Å}_{Si2-Si2}$ = 0.29). These bonds were previously introduced in Figure 2 and are presented again using solid red sticks in Figure 4 (additional information is available in Table S4). It is worth noting that these $ICOBI_{Si-Si}$ values are smaller than those previously reported for other ternary rare-earth silicides, i.e., $ICOBI_{Si-Si}$ of 0.72 and 0.66 in Y_2LiSi_2 and Sc_2AlSi_2.[68] The obtained ICOBI for longer Si−Si contacts (d > 2.52 Å, see Table S4), indicated by dashed red sticks in Figure 4, reveals a non-negligible covalent character. Therefore, (1*b*)Si dumbbells and isolated (0*b*)Si atoms build up infinite linear chains parallel to the *c*-axis ($ICOBI(tP40)^{2.90\ Å}_{Si2-Si2}$ = 0.26, $ICOBI(mS40)^{2.74\ Å}_{Si2-Si2}$ = 0.27, $ICOBI(oI40)^{2.80\ Å}_{Si2-Si2}$ = 0.26), while the zigzag fragments may be viewed as chains of silicon triangles sharing two vertices ($ICOBI(tP40)^{2.71\ Å}_{Si1-Si1}$ = 0.27, $ICOBI(mS40)^{2.73\ Å}_{Si1-Si4}$ = 0.25, $ICOBI(oI40)^{2.80\ Å}_{Si1-Si1}$ = 0.23). To provide a comprehensive description of the bonding scenario, interactions among the metal species must also be considered, as previously demonstrated for other ternary intermetallic tetrelides, particularly those involving transition metals and rare-earth elements. $ICOBI_{Y-M}$ are equal to 0.21 and 0.23 for the shortest Y−Co and Y−Fe contacts, respectively, and decrease to 0.13 for Y−Ni (see Figure 4). This lowered ICOBI value for *M* metals with increasing valence electron count is even more pronounced for the *M*−*M* interactions, decreasing from $ICOBI_{Fe-Fe}$(2.71 Å) = 0.24 to $ICOBI_{Ni-Ni}$(2.80 Å) = 0.05. This trend reveals a declining tendency of the *M* metals to covalently interact, both among themselves and with Y, following the order: Fe > Co > Ni.

At this point, it is worth providing some additional comments on the ICOBI values for the interactions under consideration. Although these values indicate a significant covalent character of the bonds, they never reach a bond order of 1.0, which would typically be expected for homopolar bonds, e.g., $ICOBI_{C-C}$ for diamond.[55] This behavior can be ascribed both to ionic contributions, making several polar covalent interactions, and to the delocalized nature of the bonding in metallic compounds. To support this interpretation, several three-center ICOBI$^{(3)}$ were calculated for different atomic triads (see Table S5).[66] The results, which range from approximately 0.046 to −0.031, indeed indicate a tendency toward delocalized bonding, even though the effect is rather small and certainly less decisive than the regular two-center interactions.

Having discussed the nature of chemical bonding in (*tP*40)$Y_2Fe_3Si_5$, (*mS*40)$Y_2Co_3Si_5$, and (*oI*40)$Y_2Ni_3Si_5$, it is of interest to extend the analysis to the other $Y_2M_3Si_5$ compounds (*M* = Mn, Cu, Tc−Pd, Re−Pt), with particular attention devoted to identifying the key chemical factors that influence crystallization into a specific structure type depending on the *M* metal. To this aim, IpCOHP% proved particularly effective and suitable for identifying trends as a function of both the *M* metal and the crystal structure. As an example, the corresponding results for the previously analyzed phases (*M* = Fe, Co, Ni) are reported in Table 2. The trends observed, including also the other *M* metals, are discussed in the following section.

Extension of the Bonding Analysis to the $Y_2M_3Si_5$ (*M* = Mn−Cu, Tc−Pd, Re−Pt) Series. Total energies obtained after structural relaxations for the $Y_2M_3Si_5$ compounds (*M* =

https://doi.org/10.1021/acs.inorgchem.5c03309
Inorg. Chem. 2025, 64, 21067−21075

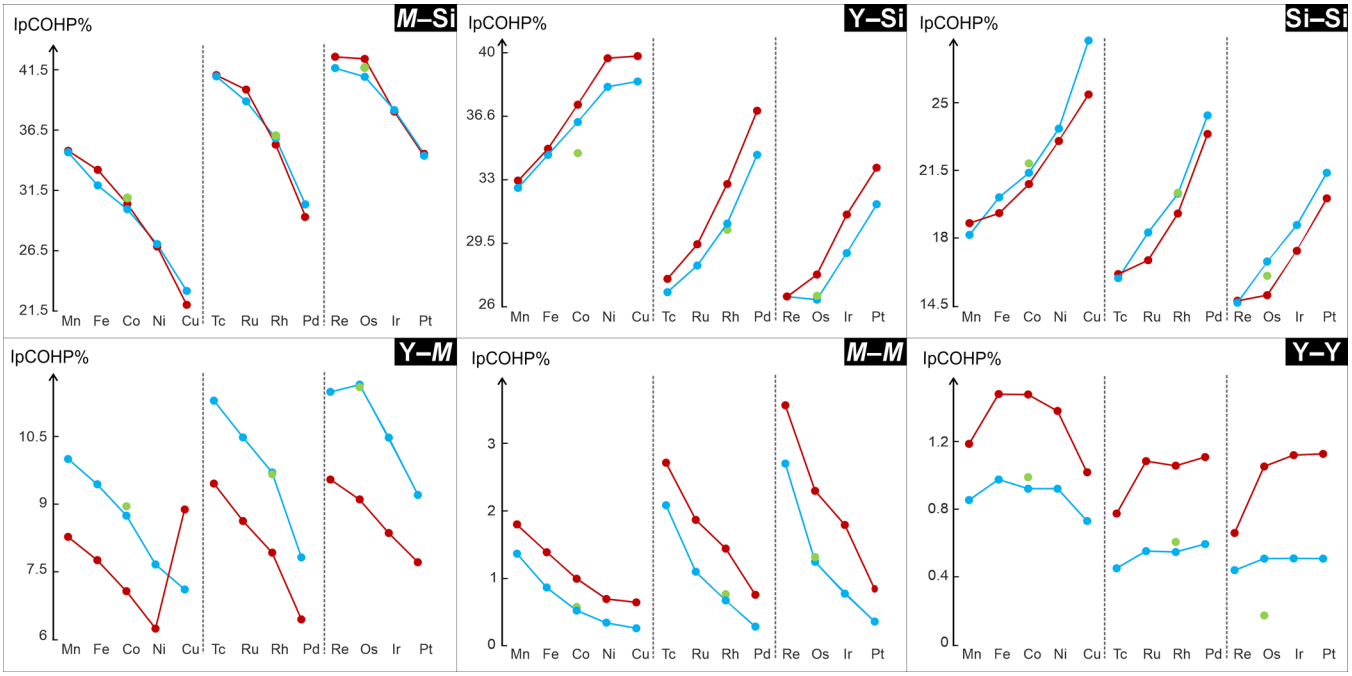

Figure 5. IpCOHP% vs transition metal (M), ordered by period. The type of interaction considered is indicated in the top-right corner of each panel. Dark red, light blue, and green dots correspond to the data for the *tP*40, *oI*40, and *mS*40 structure types, respectively. The segmented lines serve as eye guides to highlight trends as M varies.

Mn−Cu, Tc−Pd, Re−Pt) show that the *tP*40 structure is the most stable for Mn and Fe groups, *mS*40 for the Co group, and *oI*40 for the Ni group and Cu. Interestingly, for M = Mn−Ni, Ru, Rh, and Re−Ir, the lowest energy structures agree with those experimentally found (see Figure 1). While no information is available on the existence of $Y_2M_3Si_5$ with M = Tc, Pt, and Cu, recent investigations performed in our group reveal that $Y_2Pd_3Si_5$ does not form.[69] The (*mS*40)$Y_2M_3Si_5$ structure is retained upon relaxation only for M = Os, Co, and Rh, as in the other cases, it transforms into the *oI*40 type, a transition facilitated by the direct group−subgroup relationship between the two structures (see Figure S1).[27]

However, to highlight trends as a function of both the crystal structure and M, quantum−chemical calculations and analyses were performed for all obtained structures, including those not thermodynamically stable (Table S4). As anticipated, IpCOHP % proved particularly suitable for this purpose.

The periodic nature of the IpCOHP% for each type of interaction, across both groups and periods, is clearly visible in Figures 5 and S2.

The largest IpCOHP% values are associated with the M−Si, Y−Si, and Si−Si interactions, with the first two always exceeding 20%, and the latter remaining above approximately 15%. These are followed by IpCOHP%(Y−M) with values ranging between about 11 and 6%. The lowest contributions to the overall bonding capacities come from the homoatomic metal−metal interactions, i.e., M−M and Y−Y, with the latter falling below 2%.

While IpCOHP%(Y−Y) does not exhibit significant trends, despite a slight decrease within the group, these interactions can be neglected due to their particularly low contributions. The IpCOHP%(M−M) is always larger for the *tP*40 modification, due to the more covalent contribution of the M1−M1 (Table S4) bonds in this structure. Moreover, they clearly decrease along the period due to the gradual filling of the d orbitals and the resulting d−d electronic repulsion. Unlike the M−M interactions, the Y−M IpCOHP% values are higher in the *oI*40 and *mS*40 structures than in the *tP*40, although they also decrease across the period. This trend supports previous findings (Figure 3g−i, purple): the variation in the number of M electrons influences the filling of bonding and antibonding states, and consequently, the strength of the Y−M bond.

The IpCOHP%(Y−Si) increases along the period and decreases down the group (Figures 5 and S2), despite the nondirect participation of the transition element in these interactions. Here, a different number of valence electrons with a smaller atomic radius of the M elements stabilizes the interactions between yttrium and silicon (Figure S3).

The Si−Si and M−Si IpCOHP% display opposite trends (Figure 5): while the former increases along the period, the latter decreases. The M−Si pCOHP curves show antibonding states above E_F that are gradually filled as the number of M valence electrons increases, thereby weakening the M−Si interactions. At the same time, Si becomes less prone to delocalize its electrons toward M, making these electrons more available to stabilize Si−Si bonds.

An interesting conclusion that can be drawn from these trends is that chemical bonding in the $Y_2M_3Si_5$ compounds is more strongly influenced by the nature of the constituent elements than by the adopted crystal structure. This is evidenced by the larger variations in IpCOHP% observed when changing the transition metal M, compared to those resulting from structural modifications.

In this context, it is worth noting that IpCOHP%(M−Si) are the only quantities displaying significant trend variations as a function of both the transition metal M and the crystal structure. Therefore, a correlation between IpCOHP%(M−Si) values and the structural preference for a given composition has been identified, as illustrated in Figure 6.

https://doi.org/10.1021/acs.inorgchem.5c03309
Inorg. Chem. 2025, 64, 21067−21075

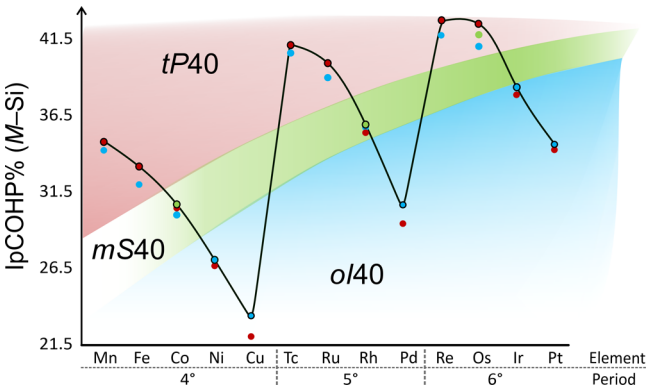

Figure 6. IpCOHP% vs transition metal (M), ordered by periods, for the M−Si interactions within each considered crystal structure. Red, green, and blue circles indicate data corresponding to the *t*P40, *m*S40, and *o*I40 structure types, respectively. The black line serves as a visual guide connecting the points with the highest IpCOHP% values for each M element. The shaded areas highlight the most stable crystal structure identified for each M.

In particular, the crystal structures identified as the most stable based on total energy calculations correspond to those exhibiting the highest IpCOHP% values for the M−Si bonds. This trend is illustrated in Figure 6 and is clearly visible by following the black line, which connects the highest IpCOHP% values for each M. It is worth reminding ourselves that total energy predictions are always consistent with experimental data, when available. This finding suggests that M−Si interactions play a dominant role in determining the crystallization into a specific structure type depending on the M metal.

CONCLUSIONS

In this work, a quantum−chemical approach was employed to investigate the chemical bonding for the $Y_2M_3Si_5$ (M = Mn−Cu, Tc−Pd, and Re−Pt) series, belonging to the broader $R_2M_3X_5$ family of intermetallic compounds. This study provides the first detailed bonding description for $Y_2M_3Si_5$ compounds (M = Fe, Co, Ni) crystallizing in three distinct but symmetry-related structure types. Through the combined use of −pCOHP curves, IpCOHP and ICOBI values, and Löwdin/QTAIM charges, the complex and mixed nature of the numerous bonding interactions was revealed. In particular, although the presence of covalent Si−Si bonds was confirmed, these were not found to be predominant, emphasizing the limitations of applying a Zintl-type formalism to these systems. Instead, the bonding scenario is dominated by polar covalent M−Si interactions, followed by the Y−Si, along with evidence of rather weak delocalized bonding from ICOBI$^{(3)}$ values. Additionally, non-negligible covalent character was also identified for the shortest Y−M and M−M contacts. The analysis was extended to the full $Y_2M_3Si_5$ (M = Mn−Cu, Tc−Pd, Re−Pt) series by simulating each composition in all three structure types regardless of their thermodynamic stability. This allowed for a comparative bonding analysis between stable and unstable configurations, enabling the identification of structure−bonding relationships. This has been achieved by comparing the IpCOHP% values for each type of interaction, highlighting their periodic trends across the transition metal series. The key finding of this analysis is that for each composition, the most stable crystal structure corresponds to the one exhibiting the highest IpCOHP% for the M−Si bonds, highlighting the dominant role of M−Si interactions. Finally, the chemical bonding investigations performed in this study will serve as a basis for future investigations of other $R_2M_3X_5$ compounds, particularly those involving different rare-earth or tetrel elements, particularly where different structures occur within the same series or where CDW-like transitions are encountered. These insights will contribute to deepening our understanding of the broader connection between the established bonding scenarios and both the chemical and physical properties of these materials.

ASSOCIATED CONTENT

Supporting Information

The Supporting Information is available free of charge at https://pubs.acs.org/doi/10.1021/acs.inorgchem.5c03309.

Data on all investigated $R_2M_3Si_5$ silicides including experimentally determined atomic positions, a Bärninghausen tree, bonding data comprising ICOHP and three-center ICOBI$^{(3)}$ values, IpCOHP% vs transition metal plots as well as COHP plots for the Y−Si interactions in $Y_2M_3Si_5$ (PDF)

AUTHOR INFORMATION

Corresponding Author

Riccardo Freccero − *Dipartimento di Chimica e Chimica Industriale, Università degli Studi di Genova, 16146 Genova, Italy;* orcid.org/0000-0003-4273-1218; Email: riccardo.freccero@unige.it

Authors

Giorgio Palla − *Dipartimento di Chimica e Chimica Industriale, Università degli Studi di Genova, 16146 Genova, Italy;* orcid.org/0009-0000-8251-9196

Linda S. Reitz − *Institute of Inorganic Chemistry, RWTH Aachen University, 52056 Aachen, Germany;* orcid.org/0009-0003-8829-9851

Serena De Negri − *Dipartimento di Chimica e Chimica Industriale, Università degli Studi di Genova, 16146 Genova, Italy;* orcid.org/0000-0002-5345-8694

Richard Dronskowski − *Institute of Inorganic Chemistry, RWTH Aachen University, 52056 Aachen, Germany;* orcid.org/0000-0002-1925-9624

Complete contact information is available at: https://pubs.acs.org/10.1021/acs.inorgchem.5c03309

Notes

The authors declare no competing financial interest.

ACKNOWLEDGMENTS

G.P. would like to thank Dr. Peter C. Müller and Dr. David Hemker for important help during this project, as they gladly provided wavefunction-based bond-order and general IT assistance. Also, discussions with PD Dr. Simon Steinberg as regards Zintl and intermetallic chemistry are gratefully acknowledged.

REFERENCES

(1) Nesper, R. Bonding Patterns in Intermetallic Compounds. *Angew. Chem., Int. Ed.* **1991**, *30* (7), 789−817.

(2) Amon, A.; Svanidze, E.; Ormeci, A.; König, M.; Kasinathan, D.; Takegami, D.; Prots, Y.; Liao, Y.-F.; Tsuei, K.-D.; Tjeng, L. H.; Leithe-

Jasper, A.; Grin, Y. Interplay of Atomic Interactions in the Intermetallic Semiconductor Be_5Pt. *Angew. Chem., Int. Ed.* **2019**, *58* (44), 15928−15933.
(3) Armbrüster, M. Intermetallic Compounds in Catalysis−a Versatile Class of Materials Meets Interesting Challenges. *Sci. Technol. Adv. Mater.* **2020**, *21* (1), 303−322.
(4) Freccero, R.; Spennati, E.; Garbarino, G.; Riani, P. Intermetallic Based Materials for Sabatier Reaction: Surface Understanding, Performance Assessment and Comparison with Commercial Catalyst. *Applied Catalysis B: Environmental* **2024**, *343*, No. 123532.
(5) Zhong, Y.; Chen, X.; Liu, S.; Liu, H.; Hu, D.; Lafaye, G.; Liang, C. Intermetallic RNi_2Si_2 (R = Ca, La, and Y) Catalysts with Electron-Rich Ni Sites for Continuous Flow Selective Hydrogenation of Maleic Anhydride. *ACS Appl. Mater. Interfaces* **2025**, *17* (4), 6175−6187.
(6) Liu, S.; Gong, Y.; Yang, X.; Zhang, N.; Liu, H.; Liang, C.; Chen, X. Acid-Durable Intermetallic $CaNi_2Si_2$ Catalyst with Electron-Rich Ni Sites for Aqueous Phase Hydrogenation of Unsaturated Organic Anhydrides/Acids. *Chinese Journal of Catalysis* **2023**, *50*, 260−272.
(7) Gong, Y.; Li, H.; Li, C.; Yang, X.; Wang, J.; Hosono, H. LaRuSi Electride Disrupts the Scaling Relations for Ammonia Synthesis. *Chem. Mater.* **2022**, *34* (4), 1677−1685.
(8) Kobayashi, Y.; Tada, S.; Mizoguchi, H. Chemical Route to Prepare Nickel Supported on Intermetallic $Ti_6Si_7Ni_{16}$ Nanoparticles Catalyzing CO Methanation. *Nanoscale* **2021**, *13* (39), 16533−16542.
(9) Mizoguchi, H.; Park, S.-W.; Kishida, K.; Kitano, M.; Kim, J.; Sasase, M.; Honda, T.; Ikeda, K.; Otomo, T.; Hosono, H. Zeolitic Intermetallics: LnNiSi (Ln = La−Nd). *J. Am. Chem. Soc.* **2019**, *141* (8), 3376−3379.
(10) Wu, J.; Li, J.; Gong, Y.; Kitano, M.; Inoshita, T.; Hosono, H. Intermetallic Electride Catalyst as a Platform for Ammonia Synthesis. *Angew. Chem., Int. Ed.* **2019**, *58* (3), 825−829.
(11) Furukawa, S.; Komatsu, T. Intermetallic Compounds: Promising Inorganic Materials for Well-Structured and Electronically Modified Reaction Environments for Efficient Catalysis. *ACS Catal.* **2017**, *7* (1), 735−765.
(12) Brown, W. K.; Plata, M. A.; Raines, M. E.; Chan, J. Y. Structural and Physical Properties of $R_2M_3X_5$ Compounds. In Bunzli, J.-C. G.; Kauzlarich, S. M., Eds.; *Handbook on the Physics and Chemistry of Rare Earths: Including Actinides*; Elsevier, 2023; *64*, 1−92.
(13) Villars, P.; Cenzual, K. *Pearson's Crystal Data: Crystal Structure Database for Inorganic Compounds, Release 2024/25*; ASM International: Materials Park, Ohio, USA, 2024.
(14) Braun, H. F. Superconductivity of Rare Earth-Iron Silicides. *Phys. Lett. A* **1980**, *75* (5), 386−388.
(15) Singh, Y.; Ramakrishnan, S. Magnetic Ordering and Superconductivity in the $R_2Ir_3Ge_5$(R = Y, La, Ce−Nd, Gd−Tm, Lu) System. *Phys. Rev. B* **2004**, *69* (17), No. 174423.
(16) Abliz, M.; Hedo, M.; Kitagawa, J.; Uwatoko, Y.; Ishikawa, M. Pressure Induced Kondo Coherence Effect. *J. Alloys Compd.* **2006**, *408−412*, 241−243.
(17) Hossain, Z.; Ohmoto, H.; Umeo, K.; Iga, F.; Suzuki, T.; Takabatake, T.; Takamoto, N.; Kindo, K. Antiferromagnetic Kondo-Lattice Systems $Ce_2Rh_3Ge_5$ and $Ce_2Ir_3Ge_5$ with Moderate Heavy-Fermion Behavior. *Phys. Rev. B* **1999**, *60* (14), 10383−10387.
(18) Mazumdar, C.; Nigam, A. K.; Nagarajan, R.; Godart, C.; Gupta, L. C.; Padalia, B. D.; Chandra, G.; Vijayaraghavan, R. Positive Giant Magnetoresistance in Antiferromagnetic $RE_2Ni_3Si_5$ (*RE*=Tb, Sm, Nd). *Appl. Phys. Lett.* **1996**, *68* (25), 3647−3649.
(19) Ramakrishnan, S.; Schönleber, A.; Rekis, T.; van Well, N.; Noohinejad, L.; van Smaalen, S.; Tolkiehn, M.; Paulmann, C.; Bag, B.; Thamizhavel, A.; Pal, D.; Ramakrishnan, S. Unusual Charge Density Wave Transition and Absence of Magnetic Ordering in $Er_2Ir_3Si_5$. *Phys. Rev. B* **2020**, *101* (6), No. 060101.
(20) Brown, W. K.; Schundelmier, B. C.; Tan, H.; Melnick, C.; Kotliar, G.; Yan, B.; Wei, K.; McCandless, G. T.; Chan, J. Y. $Sm_2Ru_3Sn_5$: A Noncentrosymmetric Cubic Member of the $Ln_2M_3X_5$ Family. *Zeitschrift für anorganische und allgemeine Chemie* **2025**, *651*, No. e202500021.
(21) Freccero, R.; De Negri, S.; Rogl, G.; Binder, G.; Michor, H.; Rogl, P. F.; Saccone, A.; Solokha, P. $La_2Pd_3Ge_5$ and $Nd_2Pd_3Ge_5$ Compounds: Chemical Bonding and Physical Properties. *Inorg. Chem.* **2021**, *60* (5), 3345−3354.
(22) Freccero, R.; Choi, S. H.; Solokha, P.; De Negri, S.; Takeuchi, T.; Hirai, S.; Mele, P.; Saccone, A. Synthesis, Crystal Structure and Physical Properties of $Yb_2Pd_3Ge_5$. *J. Alloys Compd.* **2019**, *783*, 601−607.
(23) Solokha, P.; Freccero, R.; De Negri, S.; Proserpio, D. M.; Saccone, A. The $R_2Pd_3Ge_5$ (R = La−Nd, Sm) Germanides: Synthesis, Crystal Structure and Symmetry Reduction. *Struct Chem.* **2016**, *27* (6), 1693−1701.
(24) Freccero, R.; Solokha, P.; De Negri, S. The $La_2Pd_3(Si, Ge)_5$ Complete Solid Solution: Crystal Structure, Chemical Bonding, and Volume Chemistry. *J. Alloys Compd.* **2024**, *995*, No. 174757.
(25) Dronskowski, R.; Blöchl, P. E. Crystal Orbital Hamilton Populations (COHP): Energy-Resolved Visualization of Chemical Bonding in Solids Based on Density-Functional Calculations. *J. Phys. Chem.* **1993**, *97* (33), 8617−8624.
(26) Gorelenko, Y. K.; Skolozdra, R. V.; Dutchak, Y. I.; Yarovets, V. I.; Shcherba, I. D.; Bodak, O. I. Crystal Structure X-Ray Spectra, Magnetic and Electrical Properties of $R_2Co_3Si_5$ (R = Y, Gd, Tb, Dy, Ho, Er, Tm, Lu) Compounds. *Ukrainskij Fizicheskij Zhurnal* **1985**, *30* (2), 301−304.
(27) Chabot, B.; Parthé, E. $Dy_2Co_3Si_5$, $Lu_2Co_3Si_5$, $Y_2Co_3Si_5$ and $Sc_2Co_3Si_5$ with a Monoclinic Structural Deformation Variant of the Orthorhombic $U_2Co_3Si_5$ Structure Type. *Journal of the Less Common Metals* **1985**, *106* (1), 53−59.
(28) Kyrk, T. M.; Kennedy, E. R.; Galeano-Cabral, J.; McCandless, G. T.; Scott, M. C.; Baumbach, R. E.; Chan, J. Y. Much more to explore with an oxidation state of nearly four: Pr valence instability in intermetallic m-$Pr_2Co_3Ge_5$. *Sci. Adv.* **2024**, *10*, eadl2818.
(29) Méot-Meyer, M.; Venturini, G.; Malaman, B.; Mc Rae, E.; Roques, B. Magnetisme et Conductivite Des Siliciures $Y_2Mn_3Si_5$ et $Lu_2Mn_3Si_5$. *Mater. Res. Bull.* **1985**, *20* (9), 1009−1014.
(30) Segre, C. U. *Superconductivity and Magnetism in Compounds with the $Sc_2Ru_3Si_5$-Type Structure*; Univ. of California: San Diego, CA, 1980. https://www.osti.gov/biblio/6314673.
(31) Bodak, O. I.; Pecharskii, V. K.; Gladyshevskii, E. I. Y-Re-Si system and crystal structure of certain new ternary compounds of rare earth metals. *Izv. Akad. Nauk SSSR, Neorg. Mater. (USSR)* **1978**, *14* (2), 250−255.
(32) Paccard, D.; Paccard, L. $Y_2Rh_3Si_5$, $Dy_2Rh_3Si_5$ with a Monoclinic Structural Deformation Variant of the Orthorhombic $U_2Co_3Si_5$-Type Structure. *Journal of the Less Common Metals* **1987**, *128*, 125−129.
(33) Hirjak, M.; Lejay, P.; Chevalier, B.; Etourneau, J.; Hagenmuller, P. Influence of Composition on the Structural and Superconducting Properties of the Two Polymorphic Forms of Iridium- or Silicon-Substituted YIr_2Si_2. *Journal of the Less Common Metals* **1985**, *105* (1), 139−148.
(34) Chabot, B.; Parthé, E. $Ce_2Co_3Si_5$ and $R_2Ni_3Si_5$ ($R \equiv$ Ce, Dy, Y) with the Orthorhombic $U_2Co_3Si_5$-Type Structure and the Structural Relationship with the tetragonaL $Sc_2Fe_3Si_5$-Type Structure. *Journal of the Less Common Metals* **1984**, *97*, 285−290.
(35) Patil, S.; Nagarajan, R.; Gupta, L. C.; Godart, C.; Vijayaraghavan, R.; Padalia, B. D. ^{151}Eu-Mössbauer Investigation in Some New Ternary $Eu_2M_3Si_5$ Systems (M = Ni, Pd, Cu, Rh). *Hyperfine Interact.* **1988**, *42* (1), 1063−1066.
(36) Kresse, G.; Hafner, J. Ab Initio Molecular Dynamics for Liquid Metals. *Phys. Rev. B* **1993**, *47* (1), 558−561.
(37) Kresse, G.; Furthmüller, J. Efficiency of Ab-Initio Total Energy Calculations for Metals and Semiconductors Using a Plane-Wave Basis Set. *Comput. Mater. Sci.* **1996**, *6* (1), 15−50.
(38) Kresse, G.; Furthmüller, J. Efficient Iterative Schemes for Ab Initio Total-Energy Calculations Using a Plane-Wave Basis Set. *Phys. Rev. B* **1996**, *54* (16), 11169−11186.
(39) Kresse, G.; Joubert, D. From Ultrasoft Pseudopotentials to the Projector Augmented-Wave Method. *Phys. Rev. B* **1999**, *59* (3), 1758−1775.

https://doi.org/10.1021/acs.inorgchem.5c03309
Inorg. Chem. 2025, 64, 21067−21075

(40) Hafner, J.; Kresse, G. The Vienna AB-Initio Simulation Program VASP: An Efficient and Versatile Tool for Studying the Structural, Dynamic, and Electronic Properties of Materials. *Properties of Complex Inorganic Solids*; Springer: Boston, MA, 1997.
(41) Blöchl, P. E. Projector Augmented-Wave Method. *Phys. Rev. B* **1994**, *50* (24), 17953−17979.
(42) Perdew, J. P.; Burke, K.; Ernzerhof, M. Generalized Gradient Approximation Made Simple. *Phys. Rev. Lett.* **1996**, *77* (18), 3865−3868.
(43) Monkhorst, H. J.; Pack, J. D. Special Points for Brillouin-Zone Integrations. *Phys. Rev. B* **1976**, *13* (12), 5188−5192.
(44) Pack, J. D.; Monkhorst, H. J. "Special Points for Brillouin-Zone Integrations"−a Reply. *Phys. Rev. B* **1977**, *16* (4), 1748−1749.
(45) Chevalier, B.; Lejay, P.; Etourneau, J.; Vlasse, M.; Hagenmuller, P. Structure, Superconductivity and Magnetism of New Rare Earth-Rhodium Silicides $RE_2Rh_3Si_5$ of $U_2Co_3Si_5$-Type. *Mater. Res. Bull.* **1982**, *17* (9), 1211−1220.
(46) Samsel-Czekała, M.; Winiarski, M. J. Electronic Structure of Superconducting $Lu_2Ni_3Si_5$ and Its Reference Compound $Y_2Ni_3Si_5$ by Ab Initio Calculations. *Intermetallics* **2012**, *20* (1), 63−67.
(47) Deringer, V. L.; Tchougréeff, A. L.; Dronskowski, R. Crystal Orbital Hamilton Population (COHP) Analysis As Projected from Plane-Wave Basis Sets. *J. Phys. Chem. A* **2011**, *115* (21), 5461−5466.
(48) Maintz, S.; Deringer, V. L.; Tchougréeff, A. L.; Dronskowski, R. LOBSTER: A Tool to Extract Chemical Bonding from Plane-Wave Based DFT. *J. Comput. Chem.* **2016**, *37* (11), 1030−1035.
(49) Maintz, S.; Deringer, V. L.; Tchougréeff, A. L.; Dronskowski, R. Analytic Projection from Plane-Wave and PAW Wavefunctions and Application to Chemical-Bonding Analysis in Solids. *J. Comput. Chem.* **2013**, *34* (29), 2557−2567.
(50) Nelson, R.; Ertural, C.; George, J.; Deringer, V.; Hautier, G.; Dronskowski, R. LOBSTER: Local Orbital Projections, Atomic Charges, and Chemical-bonding Analysis from Projector-augmented-wave-based Density-functional Theory. *J. Comput. Chem.* **2020**, *41* (21), 1931−1940.
(51) Tang, W.; Sanville, E.; Henkelman, G. A Grid-Based Bader Analysis Algorithm without Lattice Bias. *J. Phys.: Condens. Matter* **2009**, *21* (8), No. 084204.
(52) Henkelman, G.; Arnaldsson, A.; Jónsson, H. A Fast and Robust Algorithm for Bader Decomposition of Charge Density. *Comput. Mater. Sci.* **2006**, *36* (3), 354−360.
(53) Sanville, E.; Kenny, S. D.; Smith, R.; Henkelman, G. Improved Grid-Based Algorithm for Bader Charge Allocation. *J. Comput. Chem.* **2007**, *28* (5), 899−908.
(54) Yu, M.; Trinkle, D. R. Accurate and Efficient Algorithm for Bader Charge Integration. *J. Chem. Phys.* **2011**, *134* (6), No. 064111.
(55) Müller, P. C.; Ertural, C.; Hempelmann, J.; Dronskowski, R. Crystal Orbital Bond Index: Covalent Bond Orders in Solids. *J. Phys. Chem. C* **2021**, *125* (14), 7959−7970.
(56) Gladisch, F. C.; Steinberg, S. Revealing Tendencies in the Electronic Structures of Polar Intermetallic Compounds. *Crystals* **2018**, *8* (2), 80.
(57) Steinberg, S.; Dronskowski, R. The Crystal Orbital Hamilton Population (COHP) Method as a Tool to Visualize and Analyze Chemical Bonding in Intermetallic Compounds. *Crystals* **2018**, *8* (5), 225.
(58) Lin, Q.; Miller, G. J. Electron-Poor Polar Intermetallics: Complex Structures, Novel Clusters, and Intriguing Bonding with Pronounced Electron Delocalization. *Acc. Chem. Res.* **2018**, *51* (1), 49−58.
(59) Smetana, V.; Steinberg, S.; Mudryk, Y.; Pecharsky, V.; Miller, G. J.; Mudring, A.-V. Cation-Poor Complex Metallic Alloys in Ba(Eu)−Au−Al(Ga) Systems: Identifying the Keys That Control Structural Arrangements and Atom Distributions at the Atomic Level. *Inorg. Chem.* **2015**, *54* (21), 10296−10308.
(60) Smetana, V.; Lin, Q.; Pratt, D. K.; Kreyssig, A.; Ramazanoglu, M.; Corbett, J. D.; Goldman, A. I.; Miller, G. J. A Sodium-Containing Quasicrystal: Using Gold To Enhance Sodium's Covalency in Intermetallic Compounds. *Angew. Chem., Int. Ed.* **2012**, *51* (51), 12699−12702.
(61) Eck, B. *wxDragon*, 2020.
(62) Momma, K.; Izumi, F. VESTA 3 for Three-Dimensional Visualization of Crystal, Volumetric and Morphology Data. *J. Appl. Crystallogr.* **2011**, *44* (6), 1272−1276.
(63) Freccero, R.; Hübner, J.-M.; Prots, Y.; Schnelle, W.; Schmidt, M.; Wagner, F. R.; Schwarz, U.; Grin, Y. "Excess" Electrons in LuGe. *Angew. Chem., Int. Ed.* **2021**, *60* (12), 6457−6461.
(64) Hübner, J.-M.; Freccero, R.; Prots, Y.; Schwarz, U. The Missing Link in the Monogermanide Series: YbGe. *Chemistry−A. European Journal* **2025**, *31* (13), No. e202404515.
(65) Martinelli, A.; Ryan, D.; Sereni, J.; Ritter, C.; Leineweber, A.; Čurlík, I.; Freccero, R.; Giovannini, M. Magnetic Phase Separation in the $EuPdSn_2$ Ground State. *J. Mater. Chem. C* **2023**, *11* (23), 7641−7653.
(66) Reitz, L. S.; Hempelmann, J.; Müller, P. C.; Dronskowski, R.; Steinberg, S. Bonding Analyses in the Broad Realm of Intermetallics: Understanding the Role of Chemical Bonding in the Design of Novel Materials. *Chem. Mater.* **2024**, *36* (14), 6791−6804.
(67) Weinelt, L.; Steinberg, S. Exploring the Correlation between Chemical Bonding and Structural Distortions in $TbCu_{0.33}Te_2$. *J. Phys.: Condens. Matter* **2025**, *37* (11), 115501.
(68) Steinberg, S. Revisiting the Frontier of the Zintl−Klemm Approach for the Examples of Three Mo_2FeB_2-Type Intermetallics by Means of Quantumchemical Techniques. *Zeitschrift für anorganische und allgemeine Chemie* **2023**, *649* (18), No. e202300113.
(69) Repetto, G. Synthesis, flux growth and structural characterization of intermetallic silicides $R_2Pd_3Si_5$ (R = rare earth metal). *Master thesis*, **2025**. https://unire.unige.it/handle/123456789/11733.

https://doi.org/10.1021/acs.inorgchem.5c03309
Inorg. Chem. 2025, 64, 21067−21075